NANO LETTERS

pubs.acs.org/NanoLett Letter

Quasi-Phthalocyanine Conjugated Covalent Organic Frameworks with Nitrogen-Coordinated Transition Metal Centers for High-Efficiency Electrocatalytic Ammonia Synthesis

Minghang Jiang,[†] Linkai Han,[†] Peng Peng, Yi Hu, Yan Xiong, Chunxia Mi, Zuoxiu Tie, Zhonghua Xiang,* and Zhong Jin*

Cite This: https://doi.org/10.1021/acs.nanolett.1c04009 Read Online

ACCESS | Metrics & More | Article Recommendations | Supporting Information

ABSTRACT: Developing high-performance nitrogen reduction reaction (NRR) electrocatalysts is an ongoing challenge. Herein, we report a pyrolysis-free synthetic method for introducing ordered quasi-phthalocyanine N-coordinated transition metal (Ti, Cu, or Co) centers into a conjugated two-dimensional (2D) covalent organic framework (COF) for enhanced NRR performance. Detailed experiments and characterizations revealed that the NRR activity of Ti-COF was clearly better than that of Cu-COF and Co-COF, because of the superior abilities of Ti metal centers in activating inert N_2 molecules and suppressing the hydrogen evolution reaction (HER). The resulting Ti-COF exhibits a high NH_3 yield of 26.89 $\mu g\ h^{-1}\ mg^{-1}_{cat.}$ and a Faradaic efficiency of 34.62% for NRR. Density functional theory (DFT) calculations verify that Ti-COF can effectively adsorb and activate N_2 molecules and inhibit HER compared with Cu-COF, Co-COF, and pristine COF catalysts. This work opens a new avenue for developing 2D-COF materials that contain abundant coordinated transition metal centers toward electrocatalytic NRR.

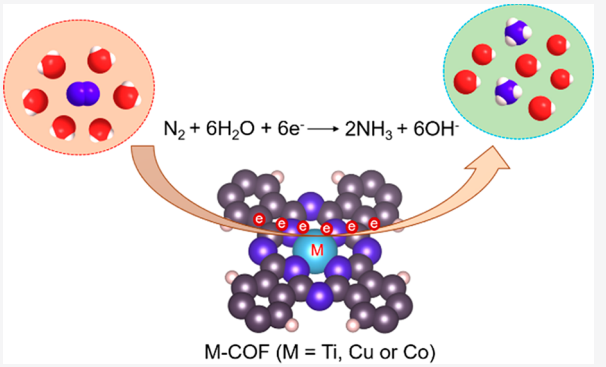

KEYWORDS: *covalent organic frameworks, N-coordinated transition metal centers, pyrolysis-free synthetic method, electrochemical nitrogen fixation*

INTRODUCTION

Ammonia (NH_3) is a basic raw material for fertilizers and other nitrogen-containing chemicals in modern industry and agriculture.[1] To date, industrial-scale ammonia production has been monopolized by the traditional Haber−Bosch process under harsh reaction conditions (650−750 K and 200−350 atm). This process takes 1−2% of the global annual energy consumption and results in >1% of worldwide greenhouse gas emissions.[2] In contrast, an environmentally friendly process that would provide sustainable ammonia production is the electrochemical N_2 reduction reaction (NRR) powered by renewable electricity under ambient conditions.[3,4] However, the electrochemical NRR process is hindered by the high activation barrier of the N_2 molecules and the vigorous competition with the HER.[5,6] Therefore, designing highly effective electrocatalysts with sufficient activity and selectivity for the NRR is of great significance.

At present, considerable research is devoted to promoting the electrochemical NRR process by using transition metal[7−9] and metal-free catalysts.[10] Transition metals can accept lone-pair electrons and effectively adsorb N_2 molecules while simultaneously feeding electrons back to the antibonding orbitals of N_2 for the activation of nonpolar N≡N triple bonds.[6,11−22] However, the d-orbital electrons in transition metals are also conducive to the formation of metal−H bonds, which will exacerbate the competitive HER[23−25] and decrease the nitrogen reduction selectivity.[5] Theoretical calculation studies[26−28] have shown that the use of N-coordinated transition metal center catalysts as active sites can significantly improve the NRR selectivity in comparison with the bulk metal surface because of the great suppression of the HER with the help of electronic and ensemble effects. For example, it was theoretically predicted that Ti@N_4 catalysts exhibited lower free energy for the NRR than that of other transition metal catalysts because of a strong back-bonding between the hybridized d-orbital of the metal atom and the π^* orbital of N_2.[26] On the basis of the above analysis, the use of N-coordinated Ti as active centers could be an effective method to enhance the NRR. Unfortunately, to the best of our

Received: October 19, 2021
Revised: December 8, 2021

knowledge, the application of N-coordinated Ti metal center electrocatalysts in the NRR has not been realized in experiments yet. Moreover, to date, reported methods to synthesize other N-coordinated transition metal center catalysts highly depend on high-temperature pyrolysis.[29−31] However, because of their thermodynamic instability, transition metal centers tend to diffuse and agglomerate during the pyrolysis process of precursors, such as zeolitic imidazolate frameworks (ZIFs). Therefore, it is imperative to develop a pyrolysis-free synthetic method for the fabrication of N-coordinated transition metal catalysts with high selectivity and excellent electrocatalytic activity for the NRR. Covalent organic frameworks (COFs) formed by repetitive organic molecules via strong covalent bonds provide more opportunities for the design of catalysts with abundant active sites.[32−35] Yan's group[33] reported that a boron-rich COF is beneficial for N_2 adsorption and that localized high N_2 concentration would promote the collision between N_2 molecules and the active sites, this is conducive to accelerating the NRR process. However, the anchoring of transition metal centers onto COFs has not been reported and is still to be explored for application in the electrocatalytic NRR.

Herein, we report a pyrolysis-free synthetic method to prepare a fully π-conjugated phthalocyanine-rich COF anchored with ordered N-coordinated M (M = Ti, Cu, or Co) metal centers that significantly enhancing the NRR performance (Figure 1a). The constructed M-COF consists of M quasi-phthalocyanine, forming conjugate 2D structures with a uniform distribution of N-coordinated M metal centers.

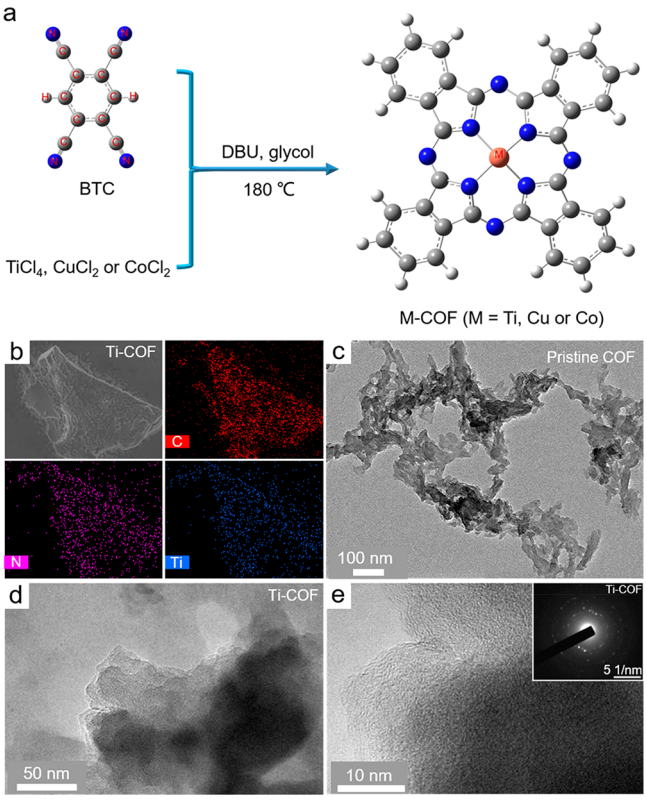

Figure 1. (a) Schematic diagram of the synthesis route for the 2D M-COF containing different ordered N-coordinated M transition metal centers (M = Ti, Cu, or Co). (b) SEM and elemental mapping images of Ti-COF. (c) TEM image of pristine COF. (d) TEM, (e) HRTEM, and (e, inset) SAED images of Ti-COF.

Among these as-constructed COFs that contain different transition metal centers, the catalytic performance of Ti-COF is clearly better than those of Cu-COF and Co-COF, which can be ascribed to the different abilities of the Ti, Cu, and Co metal centers in suppressing the HER. Density functional theory (DFT) calculations demonstrate that the introduction of Ti into the 2D COF framework can significantly inhibit HER and effectively absorb N_2 molecules, thus reducing the energy barrier for the NRR. Importantly, the proposed pyrolysis-free synthetic strategy can be extended to the synthesis of other COF-coordinated transition metal center electrocatalysts for various electrocatalysis applications.

RESULTS AND DISCUSSION

As shown in Figure 1a, the 2D M-COF (M = Ti, Cu, or Co) was prepared by the assembly of benzene-1,2,4,5-tetracarbonitrile (BTC) with M riveted in the center and finally constructed into a fully closed conjugated planar COF system. Figure S1a presents scanning electron microscopy (SEM) images of Ti-COF, exhibiting a homogeneous matrix and surface morphology without significant changes compared with that of pristine COF without the introduction of transition metal centers (Figure S1b). The corresponding elemental mappings of Ti-COF (Figure 1b) exhibit the uniform distribution of C, N, and Ti in the whole COF matrix, demonstrating that Ti-metal centers have been successfully incorporated into the COF matrix. Similarly, Cu (Figure S2) or Co (Figure S3) metal center coordinated COF samples also show that the corresponding metal centers are evenly distributed in the COF matrix, and their surface morphology has almost not changed compared with that of pristine COF (Figure S1b). Figure 1c and Figure S4a shows the field-emission transmission electron microscopy (TEM) images of pristine COF, in which a 2D laminated structure can be observed. Similarly, the TEM images of Ti-COF (Figure 1d), Cu-COF (Figure S4c), and Co-COF (Figure S4e) also present stacked sheetlike structures. This phenomenon confirms that the introduction of metal centers, including Ti, Cu, or Co, does not change the surface morphology of COF matrix. Importantly, the high-resolution transmission electron micrograph (HRTEM) images of Ti-COF (Figure 1e), Cu-COF (Figure S 4d) and Co-COF (Figure S 4f) reveal that no metal particles can be observed over the COF matrix. This result indicates that the transition metal centers (Ti, Cu, or Co) are anchored to the corresponding COF frameworks in the form of coordination structure.[34,35] As shown in the inset in Figure 1e, the selective area electron diffraction (SAED) pattern of Ti-COF exhibits several bright rings, which can be ascribed to their polycrystalline properties.

Figure 2a shows the powder X-ray diffraction (XRD) patterns of the as-prepared pristine COF, Ti-COF, Cu-COF, and Co-COF samples. The peaks in all samples at approximately 27.4° are assigned to the (003) crystalline planes of the hexagonally stacked COF.[35] In regard to the pristine COF and Cu-COF, the diffraction peaks located at 29.06° are characteristic peaks of the (013) crystalline planes of the hexagonal stack, whereas the peak at 33.60° can be indexed to the (003) planes of the orthorhombically stacked COF.[35,36] The M-COF (M = Ti, Cu, or Co) is topologically organized by quasi-phthalocyanine macrocycles and connected by closed conjugated structures (Figure S5), which is confirmed by the Raman spectra (Figure 2b and Table S1). It is worth noting that the new bands at approximately 1356

https://doi.org/10.1021/acs.nanolett.1c04009
Nano Lett. XXXX, XXX, XXX−XXX

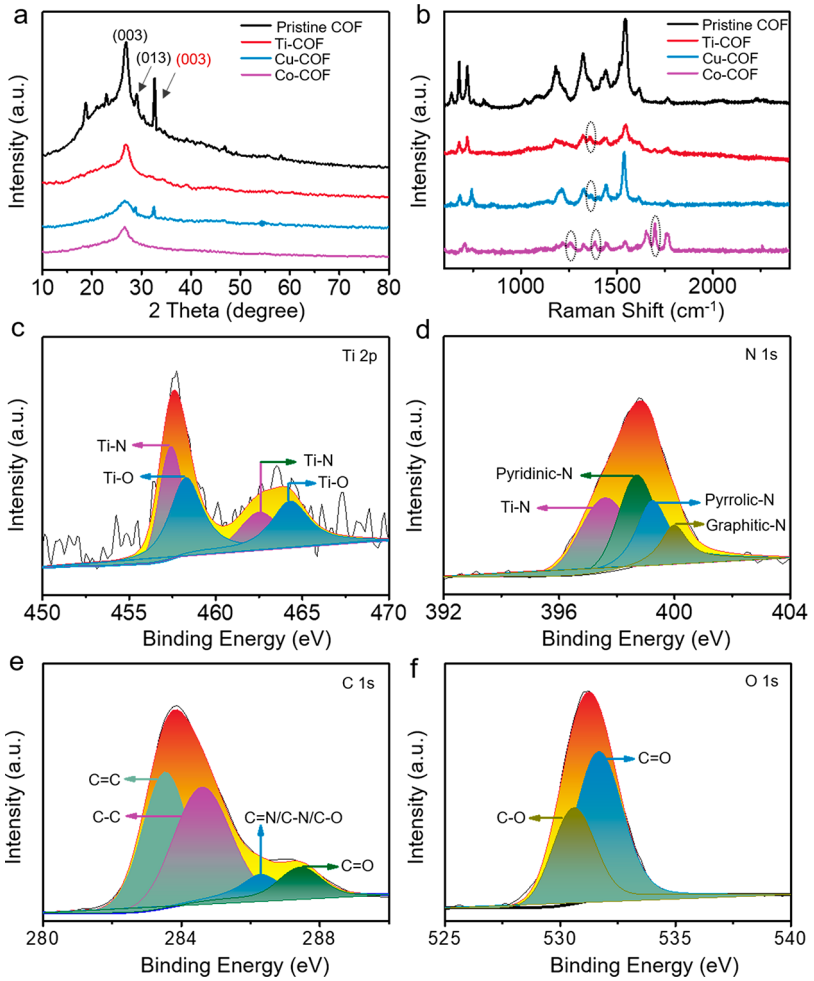

Figure 2. (a) XRD patterns of pristine COF, Ti-COF, Cu-COF, and Co-COF. (b) Raman spectra recorded with the excitation wavelength of 633 nm for pristine COF, Ti-COF, Cu-COF, and Co-COF. High-resolution XPS spectra at (c) Ti 2P, (d) N 1s, (e) C 1s, and (f) O 1s regions of Ti-COF.

cm^{-1} are formed for Ti-COF, Cu-COF, and Co-COF samples, and this band is absent for the pristine COF. These new bands are directly related to the Ti, Cu, and Co metal centers coordinated with the macrocycle rings (Figure 2b and Table S1).

The surface element compositions and detailed valence states of all catalysts were determined by X-ray photoelectron spectroscopy (XPS). The binding energies of all peaks were calibrated to the C 1s value at 284.6 eV.[37,38] Figure S6 indicate that Ti, Cu, or Co metal centers are successfully incorporated into the corresponding COF frameworks. Furthermore, the accurate mass loadings (Table S2) of metal centers in Ti-COF, Cu-COF, and Co-COF are determined by inductively coupled plasma-optical emission spectrometry (ICP-OES). Figure 2c displays the high-resolution XPS spectrum of the Ti-COF catalyst in the Ti 2p region, which can be fitted with two pairs of doublets associated with Ti−N and Ti−O bonds.[39] As shown in Figure 2d, the N 1s bands of Ti-COF located at approximately 397.56, 398.67, 399.22, and 399.98 eV are indexed to Ti-coordinated-N, pyridinic-N, pyrrolic-N, and graphitic-N, respectively.[34] The C 1s bands located at 283.53, 284.58, 287.43, and 286.29 eV of Ti-COF correspond to the typical C−C/C═C, C−N, C−O, and C═N/C═O bonds, respectively (Figure 2e). As presented in Figure 2f, the fitting curve of O 1s bands can be deconvoluted into three peaks corresponding to "Ti−O" (530.22 eV), "C−O" (530.95 eV), and "C═O" (531.74 eV) bonds.[35,40]

To preliminarily verify the electrocatalytic NRR activity, we sequentially measured the linear sweep voltammetry (LSV) curves of the same Ti-COF working electrode in Ar- and N_2-saturated 0.05 M HCl electrolytes at a scan rate of 50 mV s^{-1}. Figure 3a shows a clearly higher current density measured in the N_2-saturated electrolyte between the potential window from −0.3 to −0.8 V vs reversible hydrogen electrode (RHE), confirming the apparent catalytic activity of Ti-COF for the NRR. When more negative bias voltages were applied, the two LSV curves gradually overlapped because the competitive HER dominated the electrode process.

The catalytic activities of the samples for the NRR were evaluated in a high-purity N_2 (99.999%)-saturated 0.05 M HCl solution using a two-compartment electrochemical cell separated by a Nafion-117 ion exchange membrane (Figure S7). The as-obtained ammonia product was detected by using indophenol blue indicator, and a possible byproduct (N_2H_4) was identified by the Watt and Chrisp method.[41] Moreover, the chronoamperometry curves of Ti-COF at different working potentials are shown in Figure S8. The corresponding ultraviolet−visible light (UV−vis) absorption spectra of the product solutions stained with indophenol indicator are shown in Figure 3b. The NH_3 calibration curves are also provided in

https://doi.org/10.1021/acs.nanolett.1c04009
Nano Lett. XXXX, XXX, XXX−XXX

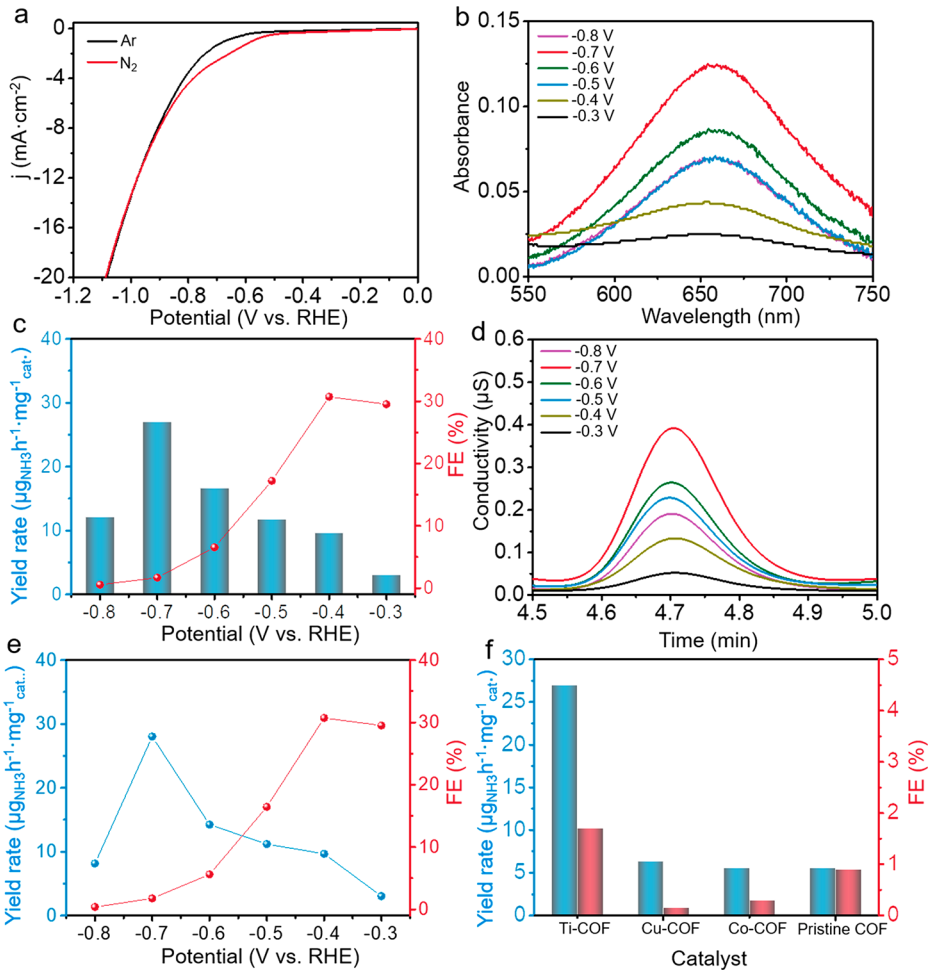

Figure 3. (a) LSV curves of Ti-COF in Ar- and N_2-saturated 0.05 M HCl electrolyte, respectively. (b) UV−vis absorption spectra of N_2-saturated 0.05 M HCl electrolyte after the NRR test of Ti-COF for 1 h and colored with an indophenol indicator. (c) Yield of NH_3 and the corresponding FE of Ti-COF at given potentials in N_2-saturated 0.05 M HCl electrolyte. (d) Ion chromatograms of N_2-saturated 0.05 M HCl electrolyte after the NRR test of Ti-COF for 1 h at a series of applied potentials. (e) Yield of NH_3 and the corresponding FE of Ti-COF detected by ion chromatography at different applied potentials. (f) Comparison of NH_3 yields and FE values of different catalysts measured at −0.7 V vs RHE.

Figure S9. Figure 3c shows that the Ti-COF electrocatalyst exhibits the highest NH_3 yield rate of 26.98 μg h^{-1} $mg^{-1}_{cat.}$ at −0.7 V and the maximum FE value of 34.62% at −0.4 V, respectively. Moreover, Figures S10 and S11 confirm the absence of N_2H_4 byproduct in the product solutions, illustrating that Ti-COF possesses good selectivity for the electroreduction of N_2 into NH_3. Moreover, the NRR performance of Ti-COF was quantitatively evaluated by ion chromatography (Figure 3d, e and Figure S12), showing the highest NH_3 yield rate (28.03 μg h^{-1} $mg^{-1}_{cat.}$) at −0.7 V and the maximum FE of 30.71% at −0.4 V vs RHE. These values are very close to the above results measured by spectrophotometry, which indicates the accuracy of the quantitative methods. At an applied potential of −0.7 V vs RHE, the NH_3 yield rate and FE of Ti-COF (26.98 μg h^{-1} $mg^{-1}_{cat.}$ and 1.7%, respectively) are significantly higher than those of Cu-COF (6.37 μg h^{-1} $mg^{-1}_{cat.}$ and 0.15%, respectively), Co-COF (5.56 μg h^{-1} $mg^{-1}_{cat.}$ and 0.3%, respectively) and pristine COF (5.55 μg h^{-1} $mg^{-1}_{cat.}$ and 0.9%, respectively) (Figure 3f). The NRR activity of Ti-COF is also higher than that of Cu-COF, Co-COF, and pristine COF catalysts at all given potentials (Figure S13). Notably, the NRR performance of Ti-COF is very competitive among the state-of-the-art electrocatalysts for NRR (Table S3). This indicates that the N-coordinated metal centers do play a positive role on improving the NRR performance, although the competitive HER process on Cu and Co metal centers reduces the NRR selectivity.

To further investigate the reasons for the varied NRR performances of the samples, we measured the electrochemical impedance spectra (EIS) of pristine COF, Ti-COF, Cu-COF, and Co-COF in N_2-saturated 0.05 M HCl solution at −0.7 V vs RHE (Figure 4a). The Nyquist curves can be fitted by the equivalent circuit (the inset of Figure 4a),[42,43] the equivalent series resistance (R_{ct}) values of Ti-COF (32.4 Ω), Cu-COF (10.0 Ω), and Co-COF (11.2 Ω) electrodes are clearly smaller than that of pristine COF electrode (57.9 Ω), indicating the lower R_{ct} and faster catalytic kinetics of M-COF than those of pristine COF. In addition, as shown in Figure S14, the C_{dl} values of Ti-COF, Cu-COF, Co-COF, and pristine COF stay at a comparable level. To further reveal the origins of the excellent catalytic activity of Ti-COF for the NRR, we compared the electrocatalytic HER performances of the samples (Figure 4b). Importantly, the Ti-COF shows much inferior catalytic activity for the HER with a much higher overpotential (1.105 V) than those of Cu-COF (0.855 V), Co-COF (0.775 V), and pristine COF (1.004 V) at 10 mA cm^{-2}.

https://doi.org/10.1021/acs.nanolett.1c04009
Nano Lett. XXXX, XXX, XXX−XXX

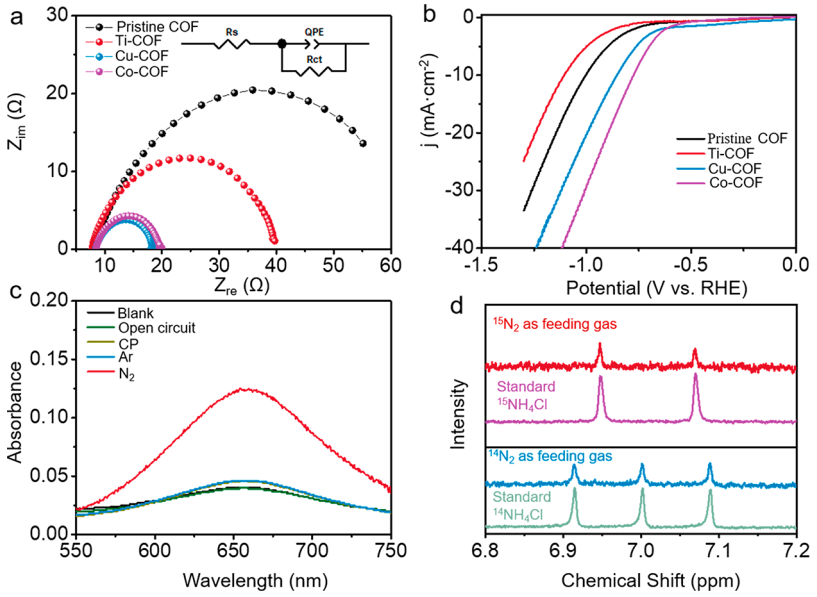

Figure 4. (a) Nyquist plots of pristine COF, Ti-COF, Cu-COF, and Co-COF in N_2-saturated 0.05 M HCl solution at −0.7 V vs RHE. (b) LSV curves of the samples for the HER in Ar-saturated 0.05 M HCl solution. (c) UV−vis absorption spectra of the electrolyte after the electrolysis at −0.7 V for 1 h under different conditions for the Ti-COF catalyst and pristine carbon paper (CP) colored by an indophenol indicator. (d) ^{1}H NMR spectra of the standard $^{14}NH_4Cl$ and $^{15}NH_4Cl$ samples and the electrolyte after the electrolysis at −0.7 V using $^{14}N_2$ or $^{15}N_2$ as the feeding gas.

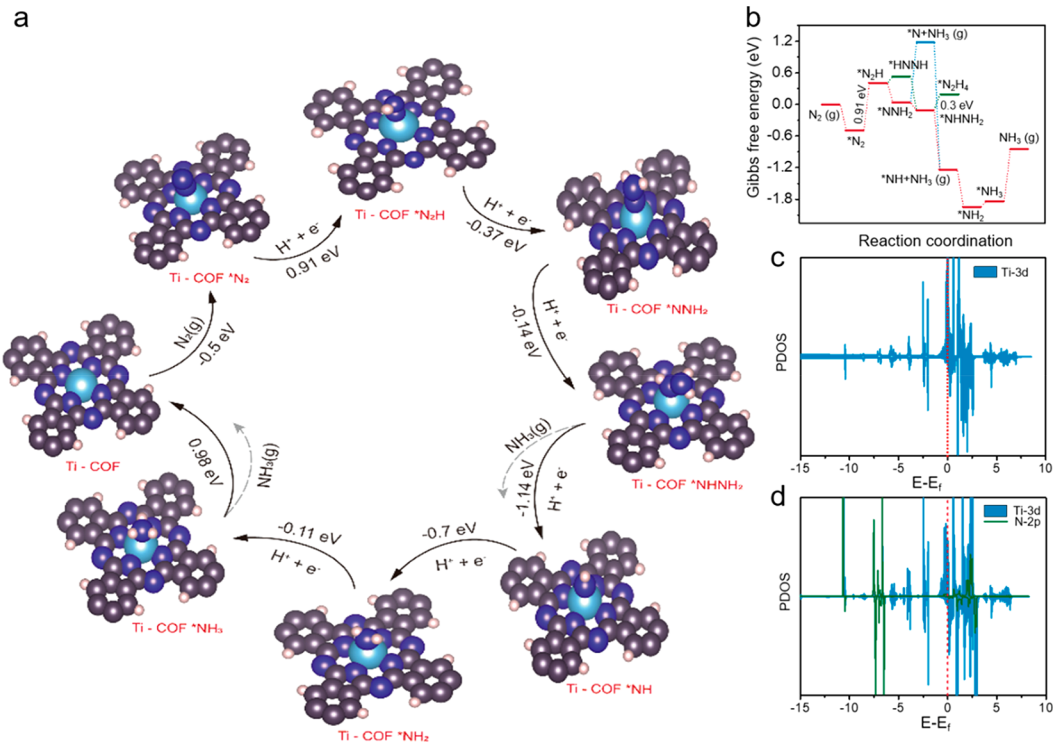

Figure 5. (a) Schematic diagram of a possible reaction mechanism for electrochemical reduction of N_2 to NH_3 on Ti-COF. (b) Free energy diagrams of possible N_2 fixation pathways on Ti-COF. (c) PDOS of Ti(3d) before N_2 adsorption on Ti-COF. (d) PDOS of Ti(3d) and *N_2(2p) after N_2 adsorption on Ti-COF.

These analysis results demonstrate that the introduction of Ti-metal centers into the 2D COF scaffold can suppress the competitive HER and thus is conducive to the NRR process.

To verify the source of NH_3 product, we executed a series of comparative experiments at the optimal potential of −0.7 V. Specifically, a control experiment of the NRR in an Ar-saturated 0.05 M HCl solution did not generate a detectable amount of NH_3, which is the same as for the blank electrolyte (Figure 4c). In addition, there was no NH_3 product by replacing the Ti-COF electrode with bare carbon paper. Moreover, the Ti-COF electrolyzed in a N_2-saturated 0.05 M HCl solution at the open-circuit potential (OCP) also generated no NH_3 product. In addition, Figure 4d shows that the typical double peaks of $^{15}NH_4^+$ species are detected

https://doi.org/10.1021/acs.nanolett.1c04009
Nano Lett. XXXX, XXX, XXX−XXX

after the continuous bubbling of $^{15}N_2$ gas (98% enrichment, Figure S15), whereas $^{14}N_2$ as the nitrogen source generate a triplet coupling peak assigned to $^{14}NH_4^+$ species. The above results indicate that the NH_3 product is derived from the electroreduction of N_2 on the M-COF catalyst. Moreover, Figures S16 and 17 indicate the good performance and structure stability of the Ti-COF catalyst during a long-term catalysis test.

To identify the intrinsic active sites and understand the NRR mechanism, we performed DFT calculations on the electrocatalytic process. There are five possible adsorption sites of N_2 for M-COF (M = Ti, Cu, or Co) and pristine COF (Figure S18a). According to DFT calculation, the lowest adsorption energy (ΔE) for N_2 is −0.97 eV on Ti-COF, which is more negative than those of the other catalysts, including Cu-COF (−0.07 eV), Co-COF (−0.03 eV), and pristine COF (−0.09 eV) (Table S4). The comparative results indicating that Ti-COF can effectively activate inert N_2 molecules and promote the NRR compared with Cu-COF, Co-COF, and pristine COF catalysts, which is consistent with the experimental test results.

Figure S18b and Table S5 shows that the Ti metal center is more conducive to adsorbing $*N_2$ rather than *H. Figure S19 shows the structure model of all reaction intermediates on Ti-COF. As shown in panels a and b in Figure 5, the preferable pathway for ammonia synthesis on Ti-COF is $*N_2 \rightarrow *N_2H \rightarrow *NNH_2 \rightarrow *NHNH_2 \rightarrow *NH+NH_3 \rightarrow *NH_2 \rightarrow *NH_3 \rightarrow NH_3$. The ΔG for nitrogen activation ($N_2 \rightarrow *N_2$) on Ti-COF is −0.5 eV, indicating that the Ti-COF has excellent nitrogen activation capability. In this dominant reaction pathway, the highest energy barrier occurs in the $*N_2 \rightarrow *N_2H$ step, and the energy barrier is 0.91 eV (Figure 5b). In contrast, the energy barrier (0.3 eV) for the formation of $*N_2H_4$ is higher (Figure 5b), which suggests that the formation of hydrazine ($*N_2H \rightarrow *NNH_2 \rightarrow *NHNH_2 \rightarrow *N_2H_4$) is difficult. Moreover, the formation of $*N+NH_3(g)$ undergoes the highest energy barrier, suggesting that the NRR process on Ti-COF follows an associative mechanism base on an alternating pathway, rather than a distal pathway.[44]

We further analyzed the electronic structure information on M-COF (M = Ti, Cu, or Co) and calculated the d-band centers and Bader charge transfer of the metal centers (Table S6). The d-band centers of Cu (−3.22) and Co (−0.92) are more negative than that of Ti (0.63). The more negative the d-band center means that the antibonding orbital of the metal center and N_2 will be in the occupied state, which is not conducive to adsorption of reactive species. This is the reason the Ti metal center has a stronger adsorption and activation ability for N_2 than those of Co and Cu. We also compared the partial density of states (PDOS) of Ti-COF before and after nitrogen activation and analyzed the orbital coupling information on Ti(3d) and $*N_2(2p)$ (Figure 5c, d). In Figure 5c, there is an area above and below $E - E_f$ where the Ti(3d) and $*N_2(2p)$ orbitals are mostly overlapped. The upper region can be regarded as an antibonded state, and the lower region can be regarded as a bonded state. Most of the antibonded states are located above $E - E_f$, which is beneficial to facilitating the adsorption of reactive species. In addition, the interaction between the metal center and the COF will cause an electron transfer from the metal centers to the COF. With an increase in the number of electrons transferred, the M-COF structure is more stable, and the charge of the metal center becomes more positive. The positive charge on the metal center prevents H ions from approaching the metal center to form *H adsorption, whereas the positive charge will promote the adsorption of N_2 on the metal centers. Moreover, the positive charge of the Ti center (+1.67 e^{-1}) is higher than that of Cu (+0.91 e^{-1}) and Co (+1.01 e^{-1}) (Table S6), which is conducive to the NRR. Meanwhile, the charge on the Ti center changed from +1.67 e^{-1} to +2.29 e^{-1} when comparing the charge state of Ti before and after nitrogen adsorption. This result indicates that there is a charge transfer between Ti and $*N_2$, which proves the formation of a chemical bond between Ti and $*N_2$. On the basis of the above DFT analysis, we can conclude that the Ti-COF structure can effectively adsorb and activate N_2 molecules, which is conducive to the occurrence of the NRR process.

CONCLUSIONS

In summary, we demonstrate the successful preparation of 2D-COFs anchored with ordered N-coordinated M (M = Ti, Cu, or Co) metal centers by a pyrolysis-free synthetic method. Benefiting from the abundant N-coordinated metal centers (especially Ti centers) constructed on the COF, the activation of inert N_2 molecule could be effectively promoted and the occurrence of the HER could be effectively suppressed. Compared to the Cu-COF, Co-COF, and pristine COF catalysts, the Ti-COF exhibited the highest catalytic activity and selectivity (no N_2H_4 is detected) for the electrocatalytic NRR. DFT calculations verified the presence of an enhanced positive charge distribution and a reduced energy barrier on Ti center, which is conducive to the activation of intermediates for facilitating the NRR process. The proposed pyrolysis-free synthesis method is a general method and can be extended to the synthesis of other transition metal center coordinated COF materials, thus opening a new avenue for the wide applications of metal-coordinated COF catalysts in clean and efficient catalysis fields.

ASSOCIATED CONTENT

Supporting Information

The Supporting Information is available free of charge at https://pubs.acs.org/doi/10.1021/acs.nanolett.1c04009.

Experimental and DFT calculation details; SEM, TEM, elemental mapping, and XPS characterizations of Cu-COF, Co-COF, and pristine COF control samples; apparatus setup for the electrochemical NRR; and electrochemical NRR performance characterizations of Cu-COF, Co-COF, and pristine COF control samples (PDF)

AUTHOR INFORMATION

Corresponding Authors

Zhonghua Xiang − *Beijing Advanced Innovation Center for Soft Matter Science and Engineering, State Key Laboratory of Organic−Inorganic Composites, Beijing University of Chemical Technology, Beijing 100029, China*; Email: xiangzh@mail.buct.edu.cn

Zhong Jin − *MOE Key Laboratory of Mesoscopic Chemistry, MOE Key Laboratory of High Performance Polymer Materials and Technology, Jiangsu Key Laboratory of Advanced Organic Materials, School of Chemistry and Chemical Engineering, Nanjing University, Nanjing, Jiangsu 210023, China; Shenzhen Research Institute of Nanjing University, Shenzhen 518063, China*; orcid.org/0000-0001-8860-8579; Email: zhongjin@nju.edu.cn

https://doi.org/10.1021/acs.nanolett.1c04009
Nano Lett. XXXX, XXX, XXX−XXX

Authors

Minghang Jiang − *MOE Key Laboratory of Mesoscopic Chemistry, MOE Key Laboratory of High Performance Polymer Materials and Technology, Jiangsu Key Laboratory of Advanced Organic Materials, School of Chemistry and Chemical Engineering, Nanjing University, Nanjing, Jiangsu 210023, China; Shenzhen Research Institute of Nanjing University, Shenzhen 518063, China*

Linkai Han − *Beijing Advanced Innovation Center for Soft Matter Science and Engineering, State Key Laboratory of Organic−Inorganic Composites, Beijing University of Chemical Technology, Beijing 100029, China*

Peng Peng − *Beijing Advanced Innovation Center for Soft Matter Science and Engineering, State Key Laboratory of Organic−Inorganic Composites, Beijing University of Chemical Technology, Beijing 100029, China*

Yi Hu − *MOE Key Laboratory of Mesoscopic Chemistry, MOE Key Laboratory of High Performance Polymer Materials and Technology, Jiangsu Key Laboratory of Advanced Organic Materials, School of Chemistry and Chemical Engineering, Nanjing University, Nanjing, Jiangsu 210023, China; Shenzhen Research Institute of Nanjing University, Shenzhen 518063, China*

Yan Xiong − *MOE Key Laboratory of Mesoscopic Chemistry, MOE Key Laboratory of High Performance Polymer Materials and Technology, Jiangsu Key Laboratory of Advanced Organic Materials, School of Chemistry and Chemical Engineering, Nanjing University, Nanjing, Jiangsu 210023, China; Shenzhen Research Institute of Nanjing University, Shenzhen 518063, China*

Chunxia Mi − *Beijing Advanced Innovation Center for Soft Matter Science and Engineering, State Key Laboratory of Organic−Inorganic Composites, Beijing University of Chemical Technology, Beijing 100029, China*

Zuoxiu Tie − *MOE Key Laboratory of Mesoscopic Chemistry, MOE Key Laboratory of High Performance Polymer Materials and Technology, Jiangsu Key Laboratory of Advanced Organic Materials, School of Chemistry and Chemical Engineering, Nanjing University, Nanjing, Jiangsu 210023, China; Shenzhen Research Institute of Nanjing University, Shenzhen 518063, China*

Complete contact information is available at: https://pubs.acs.org/10.1021/acs.nanolett.1c04009

Author Contributions

[†]M.H.J. and L.K.H. contributed equally to this work. Z.J., Z.H.X., and M.H.J. conceived the idea for this study and designed the experiments. M.H.J., P.P., and C.X.M. performed the sample fabrication, electrochemical measurements, and data analysis. M.H.J., Y.H., Y.X., and Z.X.T. performed the material characterizations. L.K.H. performed the DFT calculations. M.H.J. and Z.J. wrote and revised the paper. Z.J. planned and supervised the project.

Notes

The authors declare no competing financial interest.

■ ACKNOWLEDGMENTS

This work was supported by the National Key Research and Development Program of China (2017YFA0208200), the Fundamental Research Funds for the Central Universities of China (0205-14380266), the National Natural Science Foundation of China (22022505, 21872069), the Natural Science Foundation of Jiangsu Province (BK20180008), and the Shenzhen Fundamental Research Program of Science, Technology and Innovation Commission of Shenzhen Municipality (JCYJ20180307155007589).

■ REFERENCES

(1) Good, A. Toward nitrogen-fixing plants. *Science* **2018**, *359*, 869−870.

(2) Shi, R.; Zhang, X.; Waterhouse, G.; Zhao, X.; Zhang, R. The Journey toward Low Temperature, Low Pressure Catalytic Nitrogen Fixation. *Adv. Energy Mater.* **2020**, *10*, 2000659.

(3) Chen, G.; Ren, S.; Zhang, L.; Cheng, H.; Luo, Y.; Zhu, K.; Ding, L.; Wang, H. Advances in electrocatalytic N_2 reduction-strategies to tackle the selectivity challenge. *Small Methods* **2019**, *3*, 1800337.

(4) Yu, H.; Xue, Y.; Hui, L.; Zhang, C.; Fang, Y.; Liu, Y.; Chen, X.; Zhang, D.; Huang, B.; Li, Y. Graphdiyne based metal atomic catalysts for synthesizing ammonia. *Natl. Sci. Rev.* **2021**, DOI: 10.1093/nsr/nwaa213.

(5) Zhang, L.; Ding, L.; Chen, G.; Yang, X.; Wang, H. Ammonia synthesis under ambient conditions: Selective electroreduction of dinitrogen to ammonia on black phosphorus nanosheets. *Angew. Chem.* **2019**, *131*, 2638−2642.

(6) Jin, H.; Li, L.; Liu, X.; Tang, C.; Xu, W.; Chen, S.; Song, L.; Zheng, Y.; Qiao, S. Nitrogen vacancies on 2D layered W_2N_3: A stable and efficient active site for nitrogen reduction reaction. *Adv. Mater.* **2019**, *31*, 1902709−1902716.

(7) Li, S.; Bao, D.; Shi, M.; Wulan, B.; Yan, J.; Jiang, Q. Amorphizing of Au nanoparticles by CeO_x-RGO hybrid support towards highly efficient electrocatalyst for N_2 reduction under ambient conditions. *Adv. Mater.* **2017**, *29*, 1700001−1700006.

(8) Geng, Z.; Liu, Y.; Kong, X.; Li, P.; Li, K.; Liu, Z.; Du, J.; Shu, M.; Si, R.; Zeng, J. N_2 Electrochemical Reduction: Achieving a Record-High Yield Rate of 120.9 μg_{NH3} $mg_{cat.}^{-1}$ h^{-1} for N_2 Electrochemical Reduction over Ru Single-Atom Catalysts. *Adv. Mater.* **2018**, *30*, 1803498−1803503.

(9) Wu, T.; Zhu, X.; Xing, Z.; Mou, S.; Li, C.; Qiao, Y.; Liu, Q.; Luo, Y.; Shi, X.; Zhang, Y.; Sun, X. Greatly improving electrochemical N_2 reduction over TiO_2 nanoparticles by iron doping. *Angew. Chem.* **2019**, *58*, 18449−18453.

(10) Liu, Y.; Li, Q.; Guo, X.; Kong, X.; Ke, J.; Chi, M.; Li, Q.; Geng, Z.; Zeng, J. A Highly Efficient Metal-Free Electrocatalyst of F-Doped Porous Carbon toward N_2 Electroreduction. *Adv. Mater.* **2020**, *32*, 1907690−1907696.

(11) Xue, Z.; Zhang, S.; Lin, Y.; Su, H.; Zhai, G.; Han, J.; Yu, Q.; Li, X.; Antonietti, M.; Chen, J. Electrochemical reduction of N_2 into NH_3 by donor−acceptor couples of Ni and Au nanoparticles with a 67.8% Faradaic efficiency. *J. Am. Chem. Soc.* **2019**, *141*, 14976−14980.

(12) Suryanto, B.; Wang, D.; Azofra, L.; Harb, M.; Cavallo, L.; Jalili, R.; Mitchell, D.; Chatti, M.; MacFarlane, D. MoS_2 polymorphic engineering enhances selectivity in the electrochemical reduction of nitrogen to ammonia. *ACS Energy Lett.* **2019**, *4*, 430−435.

(13) Yu, B.; Li, H.; White, J.; Donne, S.; Yi, J.; Xi, S.; Fu, Y.; Henkelman, G.; Yu, H.; Chen, Z.; Ma, T. Tuning the catalytic preference of ruthenium catalysts for nitrogen reduction by atomic dispersion. *Adv. Funct. Mater.* **2020**, *30*, 1905665−1905675.

(14) Tao, H.; Choi, C.; Ding, L.; Jiang, Z.; Han, Z.; Jia, M.; Fan, Q.; Gao, Y.; Wang, H.; Robertson, A.; Hong, S.; Jung, S.; Liu, S.; Sun, Z. Nitrogen fixation by Ru single-atom electrocatalytic reduction. *Chem.* **2019**, *5*, 204−214.

(15) Yu, H.; Wang, Z.; Yang, D.; Qian, X.; Xu, Y.; Li, X.; Wang, H.; Wang, L. Bimetallic Ag_3Cu porous networks for ambient electrolysis of nitrogen to ammonia. *J. Mater. Chem. A* **2019**, *7*, 12526−12531.

(16) Tong, W.; Huang, B.; Wang, P.; Li, L.; Shao, Q.; Huang, X. Crystal-Phase-Engineered PdCu Electrocatalyst for Enhanced Ammonia Synthesis. *Angew. Chem.* **2020**, *59*, 2649−2653.

(17) Zhao, H.; Zhang, D.; Li, H.; Qi, W.; Wu, X.; Han, Y.; Cai, W.; Wang, Z.; Lai, J.; Wang, L. Exposure of Definite Palladium Facets

Boosts Electrocatalytic Nitrogen Fixation at Low Overpotential. *Adv. Energy Mater.* **2020**, *10*, 2002131−2002136.
(18) Cheng, H.; Ding, L.; Chen, G.; Zhang, L.; Xue, J.; Wang, H. Molybdenum carbide nanodots enable efficient electrocatalytic nitrogen fixation under ambient conditions. *Adv. Mater.* **2018**, *30*, 1803694−1803700.
(19) Li, L.; Tang, C.; Xia, B.; Jin, H.; Zheng, Y.; Qiao, S. Two-dimensional mosaic bismuth nanosheets for highly selective ambient electrocatalytic nitrogen reduction. *ACS Catal.* **2019**, *9*, 2902−2908.
(20) Cheng, H.; Cui, P.; Wang, F.; Ding, L.; Wang, H. High efficiency electrochemical nitrogen fixation achieved with a lower pressure reaction system by changing the chemical equilibrium. *Angew. Chem.* **2019**, *58*, 15541−15547.
(21) Zhang, J.; Tian, X.; Liu, M.; Guo, H.; Zhou, J.; Fang, Q.; Liu, Z.; Wu, Q.; Lou, J. Cobalt-Modulated Molybdenum−Dinitrogen Interaction in MoS_2 for Catalyzing Ammonia Synthesis. *J. Am. Chem. Soc.* **2019**, *141*, 19269−19275.
(22) Hui, L.; Xue, Y.; Yu, H.; Liu, Y.; Fang, Y.; Xing, C.; Huang, B.; Li, Y. Highly efficient and selective generation of ammonia and hydrogen on a graphdiyne-based catalyst. *J. Am. Chem. Soc.* **2019**, *141*, 10677−10683.
(23) Jiang, H.; He, Q.; Li, X.; Su, X.; Zhang, Y.; Chen, S.; Zhang, S.; Zhang, G.; Jiang, J.; Luo, Y.; Ajayan, P.; Song, L. Tracking Structural Self-Reconstruction and Identifying True Active Sites toward Cobalt Oxychloride Precatalyst of Oxygen Evolution Reaction. *Adv. Mater.* **2019**, *31*, 1805127.
(24) Liu, D.; Li, X.; Chen, S.; Yan, H.; Wang, C.; Wu, C.; Haleem, Y.; Duan, S.; Lu, J.; Ge, B.; Ajayan, P.; Luo, Y.; Jiang, J.; Song, L. Atomically dispersed platinum supported on curved carbon supports for efficient electrocatalytic hydrogen evolution. *Nat. Energy* **2019**, *4*, 512−518.
(25) He, Q.; Tian, D.; Jiang, H.; Cao, D.; Wei, S.; Liu, D.; Song, P.; Lin, Y.; Song, L. Achieving Efficient Alkaline Hydrogen Evolution Reaction over a Ni_5P_4 Catalyst Incorporating Single-Atomic Ru Sites. *Adv. Mater.* **2020**, *32*, 1906972.
(26) Choi, C.; Back, S.; Kim, N.; Lim, J.; Kim, Y.; Jung, Y. Suppression of hydrogen evolution reaction in electrochemical N_2 reduction using single-atom catalysts: A computational guideline. *ACS Catal.* **2018**, *8*, 7517−7525.
(27) Seh, Z.; Kibsgaard, J.; Dickens, C.; Chorkendorff, I.; Nørskov, J.; Jaramillo, T. Combining theory and experiment in electrocatalysis: Insights into materials design. *Science* **2017**, *355*, No. eaad4998.
(28) Greeley, J.; Jaramillo, T.; Bonde, J.; Chorkendorff, I.; Nørskov, J. Computational high-throughput screening of electrocatalytic materials for hydrogen evolution. *Nat. Mater.* **2006**, *5*, 909−913.
(29) Sa, Y.; Seo, D.; Woo, J.; Lim, J.; Cheon, J.; Yang, S.; Lee, J.; Kang, D.; Shin, T.; Shin, H.; Jeong, H.; Kim, C.; Kim, M.; Kim, T.; Joo, S. A general approach to preferential formation of active Fe-N_x sites in Fe-N/C electrocatalysts for efficient oxygen reduction reaction. *J. Am. Chem. Soc.* **2016**, *138*, 15046−15056.
(30) Wang, X.; Chen, W.; Zhang, L.; Yao, T.; Liu, W.; Lin, Y.; Ju, H.; Dong, J.; Zheng, L.; Yan, W.; Zheng, X.; Li, Z.; Wang, X.; Yang, J.; He, S.; Wang, Y.; Deng, Z.; Wu, Y.; Li, Y. Uncoordinated amine groups of metal−organic frameworks to anchor single Ru sites as chemoselective catalysts toward the hydrogenation of quinoline. *J. Am. Chem. Soc.* **2017**, *139*, 9419−9422.
(31) Chen, Y.; Ji, S.; Chen, C.; Peng, Q.; Wang, D.; Li, Y. Single-atom catalysts: synthetic strategies and electrochemical applications. *Joule* **2018**, *2*, 1242−1264.
(32) Diercks, C.; Yaghi, O. The atom, the molecule, and the covalent organic framework. *Science* **2017**, *355*, No. eaal1585.
(33) Liu, S.; Wang, M.; Qian, T.; Ji, H.; Liu, J.; Yan, C. Facilitating nitrogen accessibility to boron-rich covalent organic frameworks via electrochemical excitation for efficient nitrogen fixation. *Nat. Commun.* **2019**, *10*, 1−9.
(34) Peng, P.; Shi, L.; Huo, F.; Mi, C.; Wu, X.; Zhang, S.; Xiang, Z. A pyrolysis-free path toward superiorly catalytic nitrogen-coordinated single atom. *Sci. Adv.* **2019**, *5*, No. eaaw2322.
(35) Peng, P.; Shi, L.; Huo, F.; Zhang, S.; Mi, C.; Cheng, Y.; Xiang, Z. In situ charge exfoliated soluble covalent organic framework directly used for Zn−air flow battery. *ACS Nano* **2019**, *13*, 878−884.
(36) Jin, E.; Asada, M.; Xu, Q.; Dalapati, S.; Addicoat, M.; Brady, M.; Xu, H.; Nakamura, T.; Heine, T.; Chen, Q.; Jiang, D. Two-dimensional sp^2 carbon-conjugated covalent organic frameworks. *Science* **2017**, *357*, 673−676.
(37) Feng, L.; Li, K.; Chang, J.; Liu, C.; Xing, W. Nanostructured PtRu/C catalyst promoted by CoP as an efficient and robust anode catalyst in direct methanol fuel cells. *Nano Energy* **2015**, *15*, 462−469.
(38) Jiang, M.; Li, X.; Huang, W.; Gan, M.; Hu, L.; He, H.; Zhang, H.; Xie, F.; Ma, L. Fe_2O_3@FeP core-shell nanocubes/C composites supported irregular PtP nanocrystals for enhanced catalytic methanol oxidation. *Electrochim. Acta* **2019**, *323*, 134813.
(39) Zhang, J.; Ma, L.; Gan, M.; Fu, S.; Zhao, Y. TiN@ nitrogen-doped carbon supported Pt nanoparticles as high-performance anode catalyst for methanol electrooxidation. *J. Power Sources* **2016**, *324*, 199−207.
(40) Zhou, Y.; Xie, Z.; Jiang, J.; Wang, J.; Song, X.; He, Q.; Ding, W.; Wei, Z. Lattice-confined Ru clusters with high CO tolerance and activity for the hydrogen oxidation reaction. *Nat. Catal.* **2020**, *3*, 454−462.
(41) Watt, G.; Chrisp, J. Spectrophotometric method for determination of hydrazine. *Anal. Chem.* **1952**, *24*, 2006−2008.
(42) Li, L.; Huang, W.; Lei, J.; Shang, B.; Li, N.; Pan, F. Holey nanospheres of amorphous bimetallic phosphide electrodeposited on 3D porous Ni foam for efficient oxygen evolution. *Appl. Surf. Sci.* **2019**, *479*, 540−547.
(43) Ren, G.; Hao, Q.; Mao, J.; Liang, L.; Liu, H.; Liu, C.; Zhang, J. Ultrafast fabrication of nickel sulfide film on Ni foam for efficient overall water splitting. *Nanoscale* **2018**, *10*, 17347−17353.
(44) Xue, X.; Chen, R.; Yan, C.; Zhao, P.; Hu, Y.; Zhang, W.; Yang, S.; Jin, Z. Review on photocatalytic and electrocatalytic artificial nitrogen fixation for ammonia synthesis at mild conditions: Advances, challenges and perspectives. *Nano Res.* **2019**, *12*, 1229−1249.

https://doi.org/10.1021/acs.nanolett.1c04009
Nano Lett. XXXX, XXX, XXX−XXX